

# SUPPLEMENTARY INFORMATION FOR: GEORGIA: A GRAPH NEURAL NETWORK BASED EMULATOR FOR GLACIAL ISOSTATIC ADJUSTMENT

Yucheng Lin<sup>1</sup>, Pippa L. Whitehouse<sup>1</sup>, Andrew P. Valentine<sup>2,3</sup>, and Sarah A. Woodroffe<sup>1</sup>

<sup>1</sup>Department of Geography, Durham University, Durham, DH1 3LE, UK

<sup>2</sup>Department of Earth Sciences, Durham University, Durham, DH1 3LE, UK

<sup>3</sup>Research School of Earth Sciences, The Australian National University, Acton ACT 2601, Australia

## SUPPLEMENTARY SECTION 1 RANDOM COMBINATION OF ICE MODELS

This section details the mathematical expressions used to generate a synthetic ice history based on a random combination of previous ice sheet reconstructions (Supplementary Table 1). Starting from a set of regional ice histories with ice thickness  $\mathbb{I}_i(t)$ , we generate the synthetic ice model ( $I(t)$ ) within a hierarchical framework:

$$I(t) = \sum_{i \in M} \sum_{j \in N} \mathbb{I}_i(t + \delta) W_j \quad (1)$$

where  $M$  is an array containing randomly selected indices:

$$\begin{aligned} M &= (m_1, m_2, \dots, m_n) \\ m &\sim [U(1, K)] \\ n &\sim [U(2, 6)] \end{aligned} \quad (2)$$

$U$  indicates a uniform distribution and  $[ ]$  means that all float numbers are rounded to their nearest integers.  $m$  and  $n$  control which original ice models are selected, and the number of random models being selected, respectively.  $K$  indicates the number of ice histories available for each regional ice sheet component.

$\delta$  in equation 1 is defined by:

$$\delta \sim [N(0, 2)] \quad (3)$$

This is a Gaussian random noise model that moves the whole ice history younger or older. The selected ice history  $\mathbb{I}_i(t + \delta)$  can be further expressed as:

$$\mathbb{I}_i(t + \delta) = \begin{cases} \mathbb{I}_i(25), & t + \delta > 25 \\ \mathbb{I}_i(t + \delta), & 0 \leq t + \delta \leq 25 \\ \mathbb{I}_i(0), & t + \delta < 0 \end{cases} \quad (4)$$

where 25/0 is the first/last time step of ice history used in this study.

Lastly,  $W$  is an array containing random weighting factors for combining different ice models:

$$\begin{aligned} W &= (w_1, w_2, \dots, w_K) \\ w_j &= \begin{cases} 0, & j \neq i \\ \sim Dir(\alpha), & j = i \end{cases} \\ \alpha &\sim U(0.2, 1) \end{aligned} \quad (5)$$

$Dir$  indicates a Dirichlet distribution, which is used to generate random weighting factors that fulfil the conditions  $w_j \geq 0$  and  $\sum(W) = 1$ . The concentration parameter  $\alpha$  describes the concentration of random samples; a smaller  $\alpha$  value will generate samples where the vast majority of the mass is concentrated in just a few of the values, a larger  $\alpha$  value will generate samples where the mass is more evenly distributed.

## SUPPLEMENTARY SECTION 2 WEIGHTED PRINCIPAL COMPONENT ANALYSIS OF ICE MODELS

This section details the mathematical expressions used to generate a synthetic ice history based on the weighted Principal Component Analysis (wPCA) approach. The wPCA approach is used to extract important ice morphological patterns from the initial set of reconstructions<sup>25</sup>. A weighting scheme is adopted to account for the spherical geometry of the Earth, which means

\*yucheng.lin@durham.ac.uk

Region	Model Name	Modelling Method	Reference
Global	PaleoMIST	Geomorphological evidence determined ice history assuming ice sheets are perfectly plastic and under equilibrium conditions	Gowan et al., 2021 <sup>1</sup>
	ANU	Near- and far-field GIA modelling	Lambeck et al., <sup>2-8</sup>
	ICE_6G	Near- and far-field GIA modelling	Peltier et al., 2015 <sup>9</sup>
	ICE_5G	Near- and far-field GIA modelling	Peltier 2004 <sup>10</sup>
North America	ICE-7G_NA	Near-field GIA modelling	Roy et al., 2018 <sup>11</sup>
	NAICE <sup>+</sup>	Near-field GIA modelling	Gowan et al., 2016 <sup>12</sup>
	Han_2021	Coupled ice-sheet and GIA modelling	Han et al., 2021 <sup>13</sup>
	GLAC1-D-NA*	Glacial systems modelling with Bayesian style calibration	Tarasov et al., <sup>14,15</sup>
Eurasia	BRITICE-CHRONO*	Geomorphological evidence determined ice history assuming ice sheets are perfectly plastic and under equilibrium conditions	Clark et al., 2021 <sup>16</sup>
	Patton_2017	Thermomechanical ice modelling	Patton et al., <sup>17,18</sup>
	Han_2021	Coupled ice-sheet and GIA modelling	Han et al.m 2021 <sup>13</sup>
	GLAC1-D-EUR	Glacial systems modelling with Bayesian style calibration	Tarasov et al., 2014 <sup>19,20</sup>
Antarctica	W12	Ice sheet dynamic modelling	Whitehouse et al., 2012 <sup>21,22</sup>
	ICE6G_C	Near-field GIA modelling	Argus et al., 2014 <sup>23</sup>
	GLAC1-D-ANT	Glacial systems modelling with Bayesian style calibration	Briggs et al., 2014 <sup>24</sup>

Supplementary Table 1: Ice sheet reconstructions used in this study. \*For GLAC1-D-NA, we use two ice history scenarios for the North American Ice Sheet (nn9927 and nn9894), and for BRITICE-CHRONO, we use two scenarios for the Eurasian ice sheets (1C and 1D). <sup>+</sup>Note, NAICE does not contain the Greenland Ice Sheet component.

that grid cells at different latitudes cover different areas. We apply a weighting factor to each grid cell that is proportional to its area. Using the wPCA approach, we calculate six principal components (PCs) for each ice-sheet region and time slice. This accounts for more than 99% of the variance, and hence captures most of the spatial variability. Synthetic regional ice morphology  $I(t)$  at time  $t$  can then be generated by linearly combining different PCs:

$$I(t) = \bar{I}(t) + \sum_{i=1}^6 x_i(t)V_i(t + \delta) \quad (6)$$

$$\delta \sim [N(0, 2)] \quad (7)$$

where  $\bar{I}(t)$  represents the mean ice-sheet morphology at time  $t$ ,  $x_i$  denotes the random weighting coefficient, and  $V_i(t)$  is the  $i_{th}$  PC. To represent the temporal uncertainty within the ice sheet reconstruction, we applied a Gaussian random time shift  $\delta$  (rounded to an integer, represented by square brackets) to each PC. This means that the final ice morphology can be influenced by temporally nearby PCs. The 2 ka Gaussian random time shift is selected to reflect a conservative estimate of the temporal uncertainty associated with the empirical evidence used to constrain ice history models.

To further sample the variability of ice history, we use two methods to represent the random weighting coefficient  $x_i$ , with the first method using a temporally uniform coefficient and the second method using a temporally variable coefficient (see main text Figure 1). The first method is designed to represent general uncertainty associated with overall ice volume, and the second method is designed to reflect uncertainty associated with the short-term ice-sheet response to abrupt climate change (e.g., meltwater pulses). The temporally uniform coefficients are drawn from a normal distribution with zero mean and unit standard deviation. The temporally variable coefficients are generated by creating a time series of random noise (zero mean and three unit standard deviation) and then applying a Gaussian filter (with three unit standard deviation) to smooth the temporal signal. The filtered signal is then standardised to maintain zero mean and unit standard deviation. Examples of the resulting random ice histories are given in main text Figure 1. We do not use the ice model from Han et al., (2021)<sup>13</sup> when calculating PCs for the North American and Eurasian ice sheets because it has not been calibrated to fit any empirical constraints, and this may therefore lead to unrealistic variability.

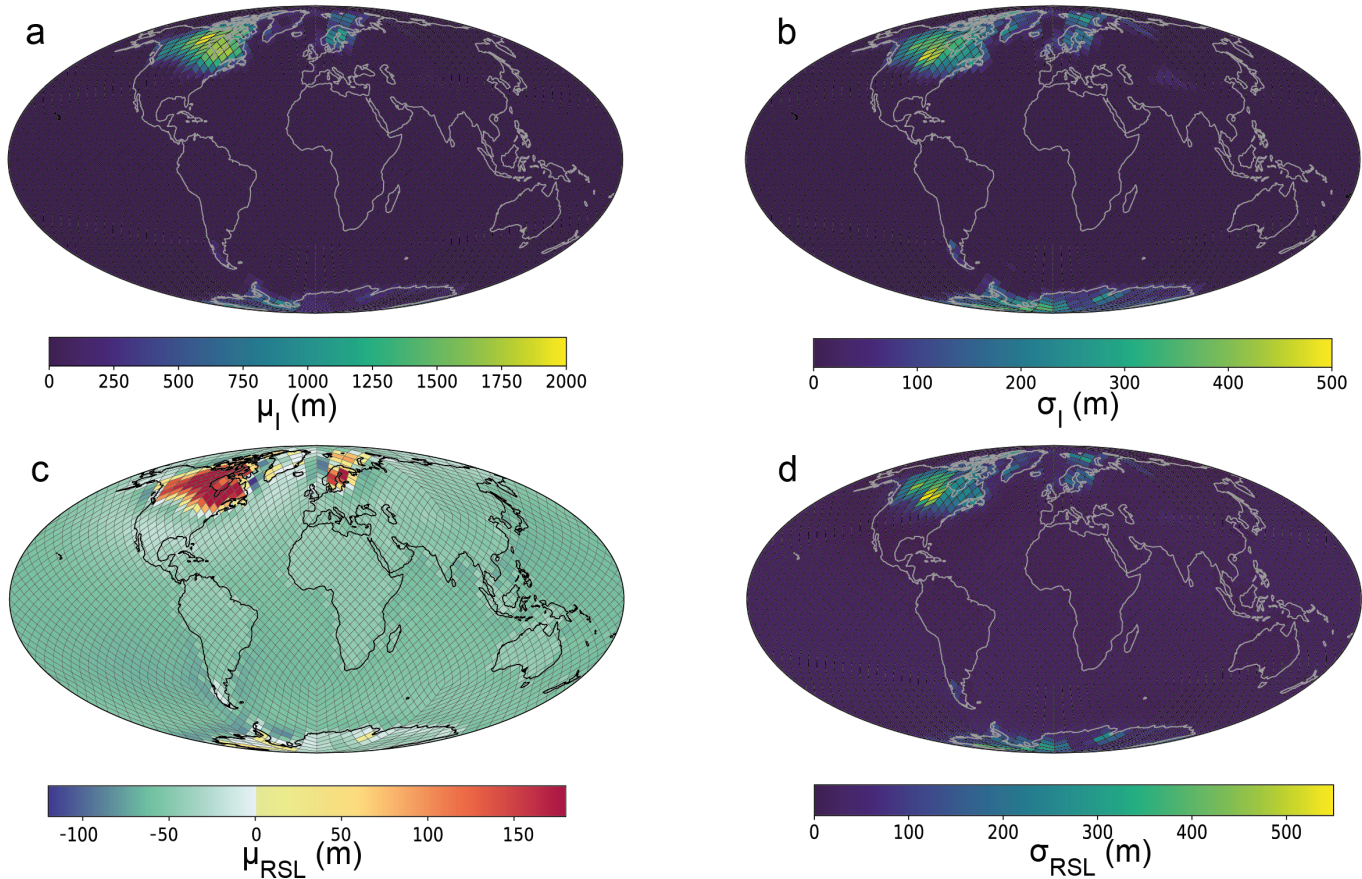
### SUPPLEMENTARY SECTION 3 DATA NORMALISATION

We normalised the input ice histories and output RSL variations using the expressions :

$$\tilde{I} = \frac{I - \mu_I}{\sigma_I} \quad (8)$$

$$R\tilde{S}L = \frac{RSL - \mu_{RSL}}{\sigma_{RSL}} \quad (9)$$

where  $I$  and  $RSL$  are 3-dimensional matrices, containing spatial and temporal information about ice thickness and RSL variation across 1,500 random examples.  $\tilde{I}$  and  $R\tilde{S}L$  are also 3-dimensional matrices representing normalised ice thickness and RSL variation values.  $\mu_I/\mu_{RSL}$  and  $\sigma_I/\sigma_{RSL}$  are 1-d arrays which contain spatial information about the mean and standard deviation of ice thickness/RSL across all time slices and random samples (see Supplementary Figure 1).



Supplementary Figure 1:  $\mu_I$ ,  $\mu_{RSL}$ ,  $\sigma_I$  and  $\sigma_{RSL}$  mentioned in Supplementary section 3. (a, b) Mean and standard deviation of ice thickness relative to present over all random ice histories and time slices. (c,d) Mean and standard deviation of relative sea-level variation induced by all random ice histories from 25 ka to present.

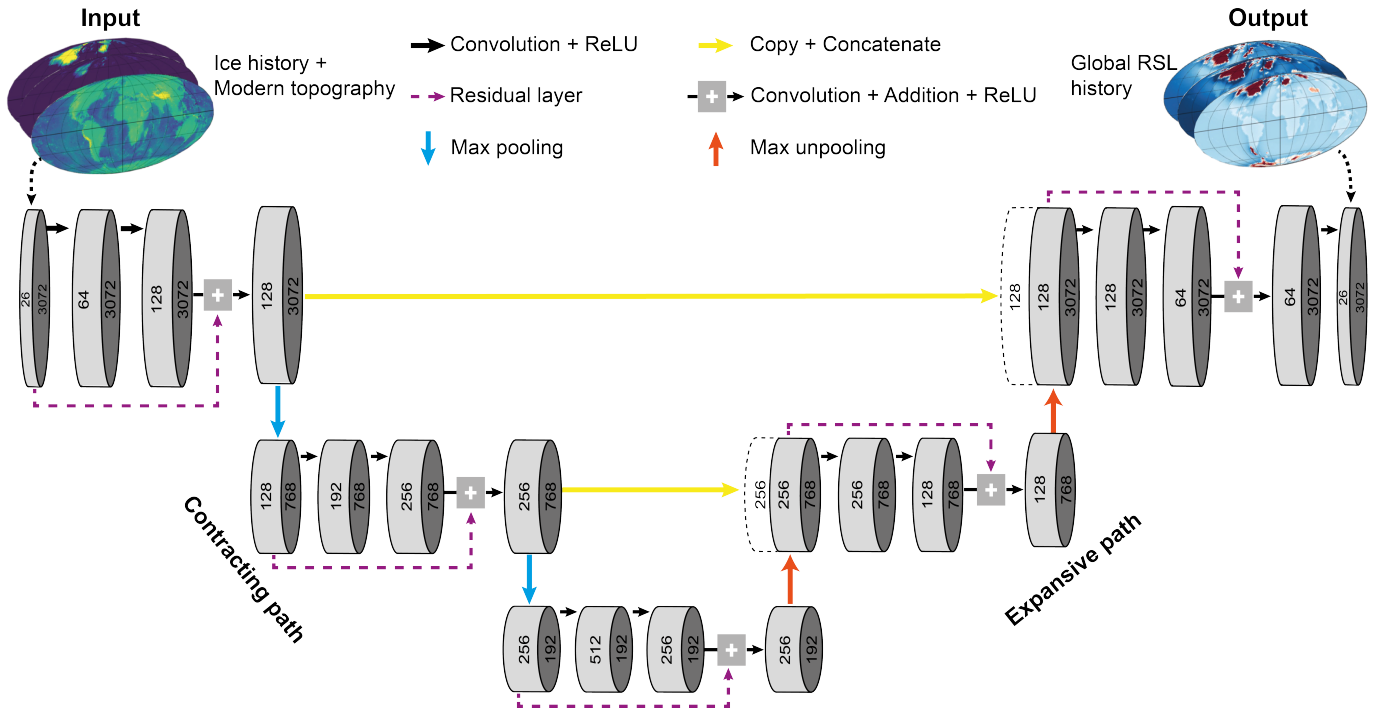
#### SUPPLEMENTARY SECTION 4 U-NET ARCHITECTURE

U-Net architecture<sup>26</sup> is a widely-used convolutional neural network architecture that has been successfully applied to regression and image segmentation problems<sup>27,28</sup>. This architecture consists of a contracting path and an expansive path (see architecture in Supplementary Figure 2). The contracting path consists of three convolution blocks with two repeated convolution operations each followed by a rectified linear unit (ReLU) activation, followed by a max pooling operation. The expansive path then processes the feature information through a sequence of max unpooling, concatenation and convolution, to produce a high resolution prediction. The pooling and unpooling processes can be easily implemented within a Healpix sampling scheme<sup>29</sup>, see Supplementary Figure 3. The concatenation operations pass the high resolution information from the contracting path to the expansive path which can effectively mitigate checkerboard artifacts in the outputs. Additionally, for each block in the contracting and expansive paths, we add a residual layer to create a shortcut for passing information from the start to the end before the ReLU activation function, which has been shown to mitigate the vanishing gradient problem for deep neural networks<sup>30</sup>.

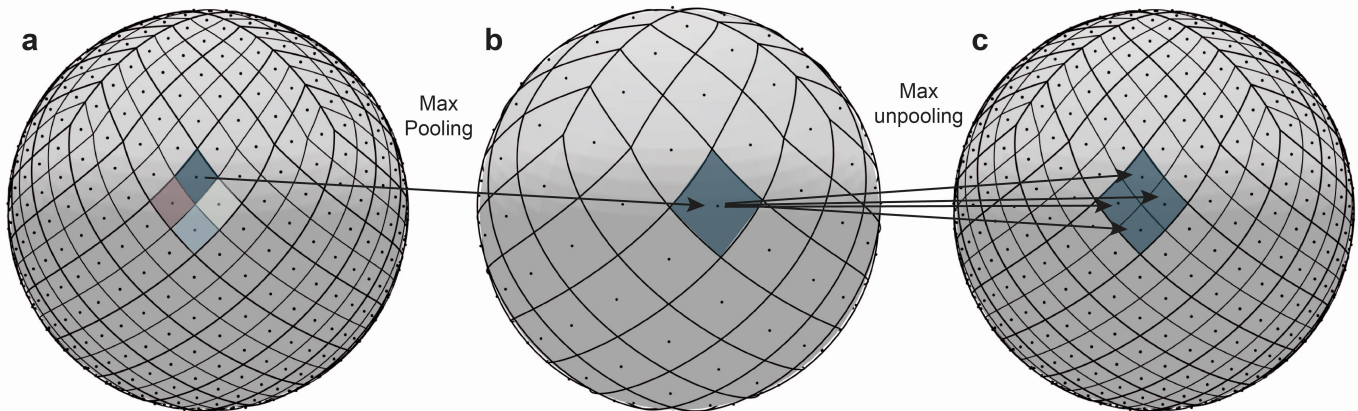
#### SUPPLEMENTARY SECTION 5 HYPERPARAMETER DEFINITION AND SELECTION CRITERIA

A full list of hyperparameters used in GEORGIA along with their definitions are given in Supplementary Table 2. In addition to some commonly-used hyperparameters, there are two hyperparameters that will directly impact the emulation performance of GEORGIA: graph filter size and U-Net depth.

Graph filter size determines the number of nearest-neighbourhoods included in each convolution process (i.e., spatial lengthscale), which is important for a GIA problem because the solid Earth deformation signal tends to be long wavelength. For example, the peripheral bulge formed in response to loading of the North American Ice Sheet can extend over 3,000 kilometres, to places like Barbados. We tested graph filter sizes of 40 and 60, corresponding to  $\sim 1500$  km and  $\sim 1780$  km radius. Because increasing the graph filter size significantly increases the number of parameters to be trained (see Supplementary Table 3), we only test graph



Supplementary Figure 2: The spherical convolutional neural network U-Net architecture. U-Net consists of a contracting path and an expansive path, which gives it a U-shaped architecture. Arrows with different colours represent different operations within the network. For each step of operation, input and output data dimension is noted. ReLU = rectified linear unit activation.



Supplementary Figure 3: Pooling and unpooling within a Hierarchical Equal Area isoLatitude Pixelization (Healpix) sampling scheme. (a) Degree-8 Healpix of the sphere,  $n = 768$ . (b) Degree-4 Healpix of the sphere ( $n = 192$ ), which can be seen as one level pooling from degree-8 Healpix. For max pooling, the maximum value within each 4-grid subdivision is assigned to the coarsened grid. (c) Same as (a) but illustrating the max unpooling process from degree-4 to degree-8 Healpix by copying the maximum value to the four grids within the original subdivision.

filter sizes up to 60. The U-Net depth defines the number of layers contained in a U-Net, where increasing the depth often enhances the capability of the model. In addition to the 3-layer U-Net shown in Supplementary Figure 2, we test a 4-layer U-Net structure, which may be helpful for extracting complex features from the inputs<sup>31</sup>. Overall, we have trained three emulators: (i) 3-layer U-Net with 40 graph filter size; (ii) 3-layer U-Net with 60 graph filter size; and (iii) 4-layer U-Net with 40 graph filter size.

Emulator performance for the 150-member unseen testing examples is summarised in Supplementary Table 3. Among the three tested emulators, emulator (ii) shows the best performance on all three metrics (mean squared error, MSE; PSNR and SSIM scores, see definitions in Supplementary section 6; Supplementary Table 3). Compared to emulator (i), emulator (ii) presents a

Model hyperparameter	Value	Parameter description
Graph filter size	60	A parameter that determines the number of nearest-neighbourhoods included in each convolution process.
U-Net depth	3	A parameter that describes the number of convolution convolution/deconvolution blocks contained within the contracting/expansive path of U-Net.
Sampling scheme	Hierarchical Equal Area isoLatitude Pixelization	This defines how a sphere is discretized.
Healpix sampling resolution	Hierarchical Equal Area isoLatitude Pixelization degree 16	This corresponds to a $\sim 3.66$ degree resolution.
Activation function	Rectified linear unit activation	A function that produces non-linearity after each node.
Optimizer	Adam	An algorithm that modifies the weights of the neural network based on the loss gradient <sup>32</sup> .
Learning rate	0.001 with a constant decay rate of 0.8 for each 100 epochs	A hyperparameter that controls how much to change the model in response to the estimated error each time the model weights are updated.
Batch size	8	The number of sub samples given to the network after which parameter update happens.
Training epoch	1500-2500 depending on the model convergence situation	A parameters that determines the total number of iterations of all the training data in one cycle for training the machine learning model.
Ensemble learning size	30	A parameters used determines how ensemble size of neural networks used to estimate predictive uncertainty.

Supplementary Table 2: Model hyperparameters used to build or train GEORGIA.

distinct improvement on the RSL misfit in near-field regions (i.e., areas beneath or near past ice-sheet boundaries), suggesting that a larger graph filter can better capture long wavelength solid-earth deformation. Interestingly, emulator (iii), which has the most trainable parameters, does not generate a better score, which may be due to the gradient vanishing and over-fitting problems found in over-deep neural networks<sup>31</sup>.

Although these three emulators contain more than 20 million trainable parameters, it takes less than 0.3 seconds to emulate RSL change through the last deglaciation (Supplementary Table 3) on a Graphics Processing Unit (GPU). The computation time increases to 3.7 seconds when using a Central Processing Unit (CPU). Because it offers the best prediction accuracy with acceptable emulation speed, we refer to emulator (ii) as GEORGIA in the main text of this paper, where it is used to carry out further analysis and produce example applications.

## SUPPLEMENTARY SECTION 6 PEAK SIGNAL-TO-NOISE RATIO AND STRUCTURAL SIMILARITY INDEX MEASURE

Peak signal-to-noise ratio (PSNR) and structural similarity index measure (SSIM) are two metrics that are widely used in measuring the quality of image and video compression<sup>33,34</sup>. Specifically, PSNR and SSIM can be expressed as:

$$PSNR = 10 \times \log_{10} \left( \frac{MAX^2}{MSE} \right) \quad (10)$$

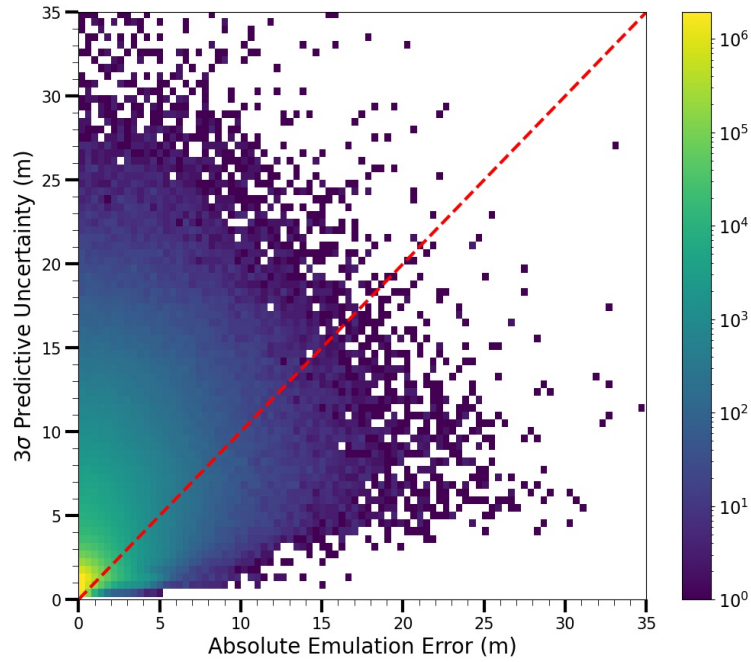
$$SSIM = \frac{1}{j^* \times T} \sum_{i=1}^{j^*} \sum_{t=1}^T \frac{(2\mu_{\hat{y}_{i,t}}^2 \mu_{y_{i,t}}^2 + c_1)(2\sigma_{\hat{y}_{i,t}y_{i,t}} + c_2)}{(\mu_{\hat{y}_{i,t}}^2 + \mu_{y_{i,t}}^2 + c_1)(\sigma_{\hat{y}_{i,t}}^2 + \sigma_{y_{i,t}}^2 + c_2)} \quad (11)$$

where MAX is the absolute maximum value among all grids with MSE indicating mean squared error, and therefore a high PSNR value indicates low noise level. For SSIM,  $\mu_{y_{i,t}}$  and  $\sigma_{y_{i,t}}$  indicate the mean and standard deviation of  $y_{i,t}$  (simulation result of a specific sample at a certain time interval) and  $\sigma_{\hat{y}_{i,t}y_{i,t}}$  is the covariance of a specific pair of emulation and simulation results.  $c_1, c_2$  are trivial values for preventing a 0 denominator. SSIM provides a similarity metric between 0 and 1 where a higher SSIM value indicates better emulation quality.

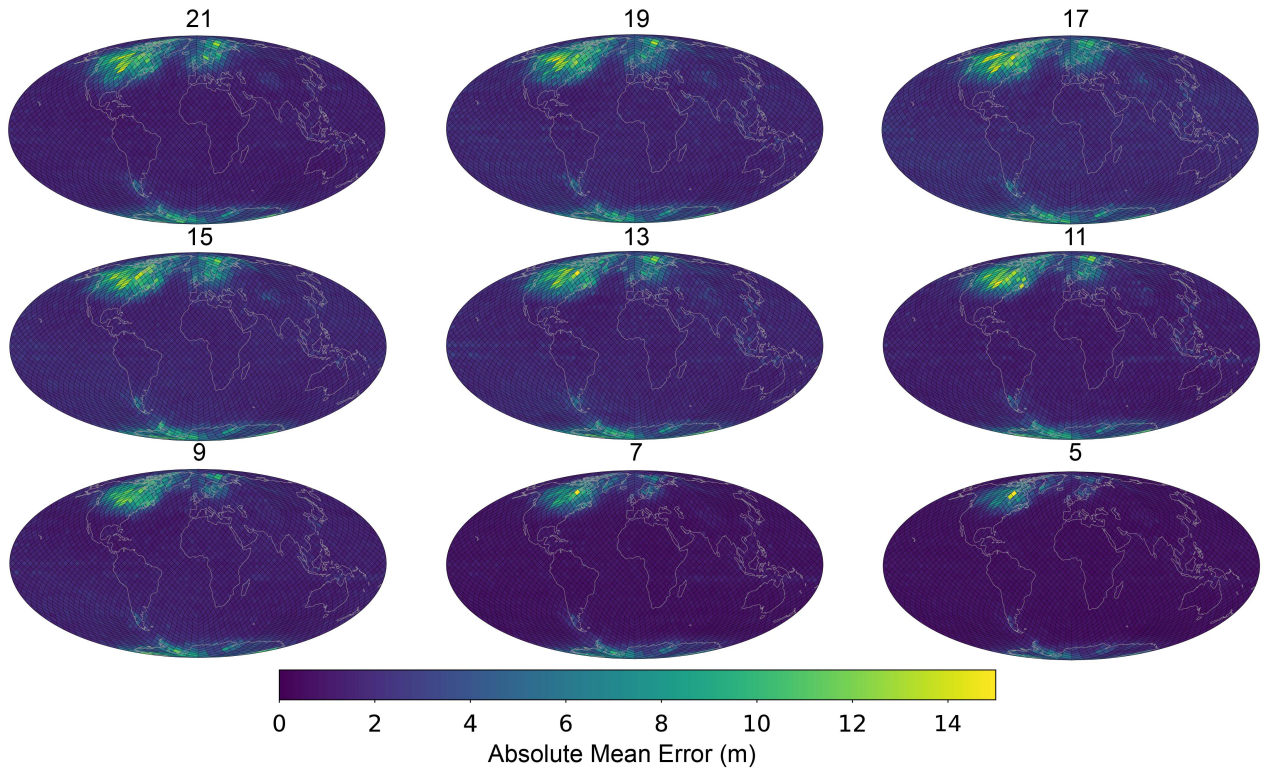
Previous studies suggest that MSE and PSNR, which are based on point-by-point comparison, can perform well in assessing the quality of noisy images, but they cannot perform well when seeking to discriminate between the structural content of images

Model Name	MSE (m <sup>2</sup> )	MAE (m)	PSNR	SSIM	Number of parameters (million)	Emulation time with GPU* (s)	Emulation time with CPU+ (s)
(i) 3-layer-40	1.184	0.73	60.15	0.9994	22.7	0.152	2.06
(ii) 3-layer-60	0.946	0.54	61.11	0.9995	33.8	0.253	3.69
(iii) 4-layer-40	1.925	0.95	58.04	0.9988	94.3	0.204	2.39

Supplementary Table 3: Evaluation of GIA emulators using the 150-member out-of-sample testing set. The three SCNN emulator names indicate the SCNN layer structure and the size of the graph filter. MSE = mean squared error; MAE = mean absolute error; PSNR = peak signal to noise ratio; SSIM = structural similarity index measure. \* The GPU used for this experiment is 8GB NVIDIA GEFORCE RTX 3070 Ti. + The CPU used for this experiment is Intel® Core™ i9 14 Core Processor.



Supplementary Figure 4: 2D histogram between absolute emulation error and  $3\sigma$  predictive uncertainty across 150-member testing set. Among them, 94.5% of  $3\sigma$  predictive uncertainties are higher than emulation error.



Supplementary Figure 5: 97.5% percentile of mean absolute emulation error across our 150-member testing set at different time steps. The time is listed above each plot with units of ka BP. This may be regarded as a conservative estimate of emulation prediction uncertainty under the assumption that unseen ice histories are from a similar distribution to our training set.

because various types of degradations applied to the same image can yield the same value of MSE and PSNR<sup>35</sup>. Conversely, SSIM is correlated with the quality and perception of the human visual system, and it can therefore better discriminate structural content across different images. Note, SSIM is not directly correlated with either MSE or PSNR, and therefore they provide independent assessments of output quality.

### SUPPLEMENTARY SECTION 7 GEORGIA INTERPOLATION PERFORMANCE

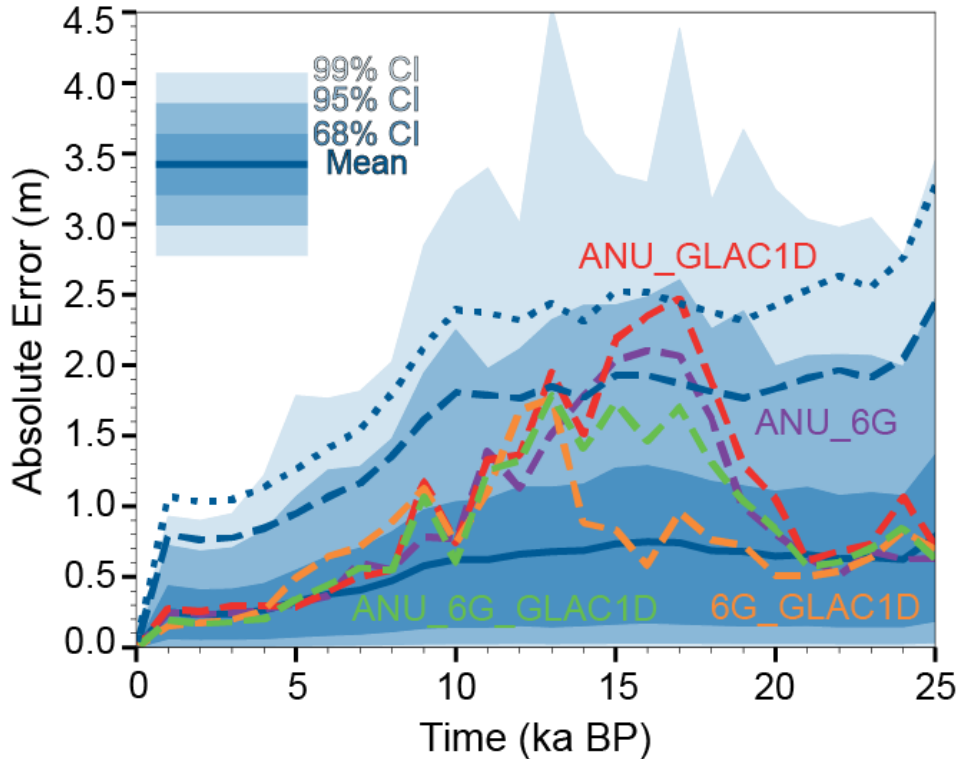
To further test GEORGIA's generalization performance regarding its ability to interpolate an unseen ice history from a similar distribution to our training set, we calculate emulation error for four synthetic North American Ice Sheet models by combining the North American component of ANU<sup>3</sup>, ICE6G\_C<sup>9</sup> and GLAC1D (nn9894 scenario<sup>14</sup>), all of which were used in the PIMP3/CMIP5 simulations<sup>36</sup>. Specifically, these four North American ice models were created by averaging ANU and ICE6G\_C, ANU and GLAC1D, ICE6G\_C and GLAC1D, and ANU, ICE6G\_C and GLAC\_1D. The temporal variation of the absolute emulation error associated with each of the four ice model is shown in Supplementary Figure 5. It can be seen that the emulation errors for all four newly-generated ice models show similar magnitude to our testing set and predictive uncertainty estimates, suggesting GEORGIA performs well in interpolation problems. In other words, GEORGIA is able to provide accurate emulation results for ice histories within the variability range of our training set.

### SUPPLEMENTARY SECTION 8 BARYSTATIC SEA-LEVEL CALCULATION

In this study, we consider barystatic sea level as a direct indicator of global grounded ice volume through time ( $BSL(t)$ ), which can be expressed as:

$$BSL(t) = -\frac{\rho_{ice}}{\rho_{water}} \left[ \frac{V_{ice}(t)}{A_{ocean}(t)} - \frac{V_{ice}(t_0)}{A_{ocean}(t_0)} \right] \quad (12)$$

where  $\rho_{ice}$  and  $\rho_{water}$  denote ice and ocean water density;  $V_{ice}(t)$  and  $A_{ocean}(t)$  represents global grounded ice volume and global ocean surface area at time  $t$ , and  $t_0$  represents the present day. To consider whether ice is grounded at each location ( $\varphi$ ) and time



Supplementary Figure 6: Temporal variation of the absolute emulation error for four synthetic ice models (represented by four coloured dotted lines). The background shows the spatially averaged, time-varying mean and confidence intervals of the emulation error and predictive uncertainty (same as Figure 2b in main text). CI = confidence interval.

( $t$ ), grounded ice volume ( $v_{ice}(t, \varphi)$ ) can be defined as:

$$V_{ice}(t) = \int v_{ice}(t, \varphi) d\varphi \quad (13)$$

$$v_{ice}(t, \varphi) = \begin{cases} 0, & i(t, \varphi) = 0 \vee i(t, \varphi) < \frac{\rho_{water}}{\rho_{ice}} b(t, \varphi) \\ v_{ice}(t, \varphi), & i(t, \varphi) \geq \frac{\rho_{water}}{\rho_{ice}} b(t, \varphi) \end{cases} \quad (14)$$

where  $i(t, \varphi)$  and  $b(t, \varphi)$  denote ice thickness and bathymetry (positive value in ocean) at location  $\varphi$  and time  $t$ , and  $b(t, \varphi)$  can be further expressed as:

$$b(t, \varphi) = b(t_0, \varphi) + RSL(t, \varphi) \quad (15)$$

where  $RSL(t, \varphi)$  indicates RSL prediction either by a physical simulator or the statistical emulator.

One important concept that should be noted is that the definition of BSL used here is a measure of global grounded ice volume, it does not reflect the magnitude of global mean sea-level rise that would occur if all grounded ice melts<sup>37</sup>. This is due to the fact that some ice-sheets are marine-ground and hence the ice volume below flotation will not contribute to global mean sea-level rise.

To calculate the effective ice thickness ( $v_{ice}^e(t, \varphi)$ ) that contributes to global mean sea-level rise, equation 14 should be re-written as:

$$v_{ice}^e(t, \varphi) = \begin{cases} 0, & i(t, \varphi) = 0 \vee i(t, \varphi) < \frac{\rho_{water}}{\rho_{ice}} b(t, \varphi) \\ v_{ice}(t, \varphi) - \frac{\rho_{water}}{\rho_{ice}} b(t, \varphi), & i(t, \varphi) \geq \frac{\rho_{water}}{\rho_{ice}} b(t, \varphi) \end{cases} \quad (16)$$

Global mean sea level can then be calculated by substituting  $v_{ice}(t, \varphi)$  with  $v_{ice}^e(t, \varphi)$  in equation 12. Based on our 1,500 forward modelling results, the difference between BSL and the magnitude of global mean sea-level rise since the Last Glacial Maximum can vary between 5 and 20 m.

## SUPPLEMENTARY REFERENCES

1. Gowan, E. J. *et al.* A new global ice sheet reconstruction for the past 80 000 years. *Nature communications* **12**, 1–9 (2021).
2. Lambeck, K., Purcell, A. & Zhao, S. The North American Late Wisconsin ice sheet and mantle viscosity from glacial rebound analyses. *Quaternary Science Reviews* **158**, 172–210 (2017).
3. Lambeck, K., Rouby, H., Purcell, A., Sun, Y. & Sambridge, M. Sea level and global ice volumes from the Last Glacial Maximum to the Holocene. *Proceedings of the National Academy of Sciences* **111**, 15296–15303 (2014).
4. Lambeck, K., Purcell, A., Zhao, J. & SVENSSON, N.-O. The Scandinavian ice sheet: from MIS 4 to the end of the last glacial maximum. *Boreas* **39**, 410–435 (2010).
5. Lambeck, K., Yokoyama, Y. & Purcell, T. Into and out of the Last Glacial Maximum: sea-level change during Oxygen Isotope Stages 3 and 2. *Quaternary Science Reviews* **21**, 343–360 (2002).
6. Lambeck, K. & Purcell, A. P. Sea-level change in the Irish Sea since the Last Glacial Maximum: constraints from isostatic modelling. *Journal of Quaternary Science: Published for the Quaternary Research Association* **16**, 497–506 (2001).
7. Lambeck, K., Smither, C. & Johnston, P. Sea-level change, glacial rebound and mantle viscosity for northern Europe. *Geophysical Journal International* **134**, 102–144 (1998).
8. Lambeck, K. Glacial rebound of the British Isles—II. A high-resolution, high-precision model. *Geophysical Journal International* **115**, 960–990 (1993).
9. Peltier, W., Argus, D. & Drummond, R. Space geodesy constrains ice age terminal deglaciation: The global ICE-6G\_C (VM5a) model. *Journal of Geophysical Research: Solid Earth* **120**, 450–487 (2015).
10. Peltier, W. R. Global glacial isostasy and the surface of the ice-age Earth: the ICE-5G (VM2) model and GRACE. *Annu. Rev. Earth Planet. Sci.* **32**, 111–149 (2004).
11. Roy, K. & Peltier, W. Relative sea level in the Western Mediterranean basin: A regional test of the ICE-7G\_NA (VM7) model and a constraint on late Holocene Antarctic deglaciation. *Quaternary Science Reviews* **183**, 76–87 (2018).
12. Gowan, E. *et al.* ICESHEET 1.0: a program to produce paleo-ice sheet reconstructions with minimal assumptions (2016).
13. Han, H. K., Gomez, N., Pollard, D. & DeConto, R. Modeling Northern Hemispheric ice sheet dynamics, sea level change, and solid Earth deformation through the last glacial cycle. *Journal of Geophysical Research: Earth Surface* **126**, e2020JF006040 (2021).
14. Tarasov, L., Dyke, A. S., Neal, R. M. & Peltier, W. R. A data-calibrated distribution of deglacial chronologies for the North American ice complex from glaciological modeling. *Earth and Planetary Science Letters* **315**, 30–40 (2012).
15. Tarasov, L. & Peltier, W. R. Greenland glacial history, borehole constraints, and Eemian extent. *Journal of Geophysical Research: Solid Earth* **108** (2003).
16. Clark, C. D. *et al.* Timing, pace and controls on ice sheet retreat: an introduction to the BRITICE-CHRONO transect reconstructions of the British–Irish Ice Sheet. *Journal of Quaternary Science* **36**, 673–680 (2021).

17. Patton, H. *et al.* Deglaciation of the Eurasian ice sheet complex. *Quaternary Science Reviews* **169**, 148–172 (2017).
18. Patton, H., Hubbard, A., Andreassen, K., Winsborrow, M. & Stroeven, A. P. The build-up, configuration, and dynamical sensitivity of the Eurasian ice-sheet complex to Late Weichselian climatic and oceanic forcing. *Quaternary Science Reviews* **153**, 97–121 (2016).
19. Tarasov, L. *et al.* The global GLAC-1c deglaciation chronology, meltwater pulse 1-a, and a question of missing ice in IGS Symposium: Contribution of Glaciers and Ice Sheets to Sea-Level Change, Chamonix, France (2014), 26–30.
20. Abe-Ouchi, A. *et al.* Insolation-driven 100,000-year glacial cycles and hysteresis of ice-sheet volume. *nature* **500**, 190–193 (2013).
21. Whitehouse, P. L., Bentley, M. J. & Le Brocq, A. M. A deglacial model for Antarctica: geological constraints and glaciological modelling as a basis for a new model of Antarctic glacial isostatic adjustment. *Quaternary Science Reviews* **32**, 1–24 (2012).
22. Whitehouse, P. L., Bentley, M. J., Milne, G. A., King, M. A. & Thomas, I. D. A new glacial isostatic adjustment model for Antarctica: calibrated and tested using observations of relative sea-level change and present-day uplift rates. *Geophysical Journal International* **190**, 1464–1482 (2012).
23. Argus, D. F., Peltier, W., Drummond, R. & Moore, A. W. The Antarctica component of postglacial rebound model ICE-6G\_C (VM5a) based on GPS positioning, exposure age dating of ice thicknesses, and relative sea level histories. *Geophysical Journal International* **198**, 537–563 (2014).
24. Briggs, R. D., Pollard, D. & Tarasov, L. A data-constrained large ensemble analysis of Antarctic evolution since the Eemian. *Quaternary Science Reviews* **103**, 91–115 (2014).
25. Domingo, D., Malmierca-Vallet, I., Sime, L., Voss, J. & Capron, E. Using ice cores and Gaussian process emulation to recover changes in the Greenland ice sheet during the last interglacial. *Journal of Geophysical Research: Earth Surface* **125**, e2019JF005237 (2020).
26. Ronneberger, O., Fischer, P. & Brox, T. *U-net: Convolutional networks for biomedical image segmentation* in *International Conference on Medical image computing and computer-assisted intervention* (2015), 234–241.
27. Lai, C.-Y. *et al.* Vulnerability of Antarctica’s ice shelves to meltwater-driven fracture. *Nature* **584**, 574–578 (2020).
28. Yao, W., Zeng, Z., Lian, C. & Tang, H. Pixel-wise regression using U-Net and its application on pansharpening. *Neurocomputing* **312**, 364–371 (2018).
29. Gorski, K. M. *et al.* HEALPix: A framework for high-resolution discretization and fast analysis of data distributed on the sphere. *The Astrophysical Journal* **622**, 759 (2005).
30. Srivastava, R. K., Greff, K. & Schmidhuber, J. Training very deep networks. *Advances in neural information processing systems* **28** (2015).
31. Goodfellow, I., Bengio, Y. & Courville, A. *Deep learning* (MIT press, 2016).
32. Kingma, D. P. & Ba, J. Adam: A method for stochastic optimization. *arXiv preprint arXiv:1412.6980* (2014).
33. Wang, Z. & Bovik, A. C. Mean squared error: Love it or leave it? A new look at signal fidelity measures. *IEEE signal processing magazine* **26**, 98–117 (2009).
34. Huynh-Thu, Q. & Ghanbari, M. Scope of validity of PSNR in image/video quality assessment. *Electronics letters* **44**, 800–801 (2008).
35. Hore, A. & Ziou, D. *Image quality metrics: PSNR vs. SSIM* in *2010 20th international conference on pattern recognition* (2010), 2366–2369.
36. Abe-Ouchi, A. *et al.* Ice-sheet configuration in the CMIP5/PMIP3 Last Glacial Maximum experiments. *Geoscientific Model Development* **8**, 3621–3637 (2015).
37. Goelzer, H., Coulon, V., Pattyn, F., De Boer, B. & Van De Wal, R. Brief communication: On calculating the sea-level contribution in marine ice-sheet models. *The Cryosphere* **14**, 833–840 (2020).